



Cite this: *Chem. Commun.*, 2025, 61, 3688

Received 20th November 2024,
Accepted 29th January 2025

DOI: 10.1039/d4cc06170e

rsc.li/chemcomm

Highly conductive composite anode catalysts featuring a fused Ir nano-network towards proton exchange membrane electrocatalysis†

Lu Zhang,^a Qiannan Wu,^{ab} Xiao Zhao,^{id}^c Xiao Liang,^a Xiaoxin Zou,^{id}^a and Hui Chen^{id*}^a

A boride-assisted method has been presented to synthesize a fused Ir nano-network supported on TiO_2 as highly conductive composite catalysts (Ir NN@TiO_2) for the reaction of oxygen evolution in acid. The Ir NN@TiO_2 can be utilized to construct an anode catalyst layer of a proton exchange membrane water electrolyzer (PEMWE) with a low iridium content of $0.3 \text{ mg}_{\text{Ir}} \text{ cm}^{-2}$. The low-iridium-loading PEMWE exhibits excellent performance, *i.e.*, 2.9 A cm^{-2} @ 1.9 V with Nafion 115 membrane, and operates stably at a current density of 1.0 A cm^{-2} for over 1000 h.

The proton exchange membrane water electrolyzer (PEMWE), which can effectively adapt to the electric instantaneous fluctuations from intermittent renewable energy sources, is emerging as a hot technology for producing green hydrogen.^{1–3} The catalyst-coated membrane (CCM), which is the central component of a PEMWE, is made up of an anode catalyst layer, cathode catalyst layer, and solid electrolyte (such as a perfluorosulfonic membrane).^{4–6} Due to the high acidity of the perfluorosulfonic membrane, noble metal-based electrocatalysts, such as platinum (Pt) and iridium (Ir) are necessary to catalyze the hydrogen evolution reaction (HER) at the cathode and the oxygen evolution reaction (OER) at the anode. At the cathode, the dispersion of Pt nanoparticles on carbonous supports (*i.e.*, Pt/C catalysts) has led to the reduction of Pt loadings down to $0.5 \text{ mg}_{\text{Pt}} \text{ cm}^2$ in a PEMWE cell.⁷ However, carbon black materials are unsuitable supports for Ir nanocatalysts at the anode, as carbon can be electrochemically oxidized at highly oxidizing potentials, leading to catalyst degradation. Consequently, the high packing density of unsupported Ir or

IrO_2 nanocatalysts results in a current Ir loading in commercial electrolyzers of $2\text{--}4 \text{ mg}_{\text{Ir}} \text{ cm}^{-2}$, which is required to generate a consistent and continuous catalyst layer.³

In order to reduce the Ir loading amount, researchers have been exploring acid-stable metal oxides, such as TiO_2 , SnO_2 and Nb_2O_5 , as potential support candidates to support Ir-based nanocatalysts.^{8,9} Some well-designed catalysts possess strong interface interaction between the oxide supports and surface iridium species to improve the intrinsic activity for the acidic OER. In three-electrode liquid-electrolyte measurements, they present better OER activity than IrO_2 , while they contain 30–50% less Ir content relative to IrO_2 .¹⁰ Despite recent efforts, few reports demonstrate the practical application of those oxide-supported catalysts in real PEMWEs *via* integrating them into CCMs. Furthermore, while several oxide-supported catalysts have been utilized to prepare the anode catalyst layer in PEMWE, they typically run for less than 200 hours at not exceeding 1 A cm^{-2} , or require high Ir loadings of over $2 \text{ mg}_{\text{Ir}} \text{ cm}^{-2}$ to achieve better CCM performance than IrO_2 .^{8,11} A serious drawback of these oxide supports is their inadequate electrical conductivity to deliver ampere-level current density in PEMWEs.^{12,13} In fact, the ideal anode catalysts in PEMWEs should have high electrical conductivity of $>0.1 \text{ S cm}^{-1}$. Therefore, the ability to enhance the conductivity of oxide-supported catalysts is of vital importance in our pursuit to develop low Ir CCMs with high activity and durability.

Herein, we propose a boride-assisted method to synthesize a highly conductive Ir nanocatalyst supported on TiO_2 (Fig. 1a), where Ir nanoparticles have fused at the junctions to create an interconnected Ir nano-network (Fig. 1b and Fig. S1–S2 in ESI† denoted hereafter as Ir NN@TiO_2). The Ir NN@TiO_2 was synthesized using a wet chemical approach, which involved the chemical reaction of TiB_2 (Fig. S3, ESI†) with H_2IrCl_6 in ethyl alcohol– H_2O mixed solution (details are provided in the Experimental section, ESI†). During the reaction, the TiB_2 was oxidized into a TiO_2 support, while IrCl_6^{2-} was reduced to elemental Ir. It is worth emphasizing that when TiO_2 was used

^a State Key Laboratory of Inorganic Synthesis and Preparative Chemistry, College of Chemistry, Jilin University, Changchun 130012, China.

E-mail: chenhui@jlu.edu.cn

^b Hefei conservation of momentum green energy Co., Ltd, Hefei, 231100, China

^c School of Materials Science and Engineering, Key Laboratory of Automobile Materials of MOE, State Key Laboratory of Automotive Simulation and Control, Electron Microscopy Center, Jilin University, Changchun 130012, China

† Electronic supplementary information (ESI) available. See DOI: <https://doi.org/10.1039/d4cc06170e>



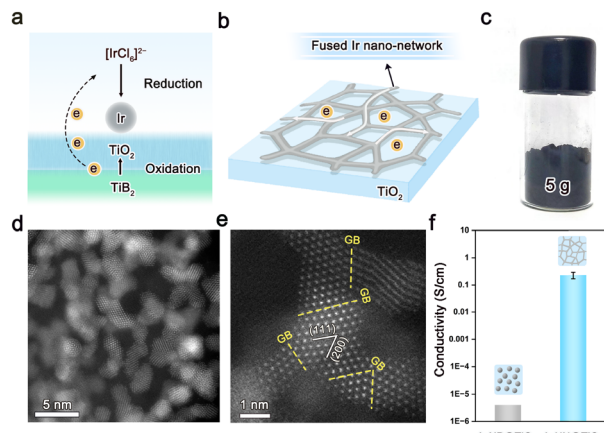


Fig. 1 (a) Synthetic preparation of Ir NN@TiO₂ based on a redox reaction of H₂IrCl₆ with TiB₂. (b) Schematic illustration of Ir NN@TiO₂ that consists of a fused Ir nano-network on TiO₂ supports. (c) Digital image of 5 g Ir NN@TiO₂ obtained from a scaled-up synthesis. (d) and (e) TEM images of Ir NN@TiO₂. (f) The comparison of the electrical conductivity for Ir NN@TiO₂ and Ir NP@TiO₂.

to replace TiB₂ in the synthesis, highly dispersed Ir nanoparticles on TiO₂ supports were formed (denoted Ir NP@TiO₂, Fig. S4, ESI[†]). This comparison indicates that TiB₂ is unique in its ability to assist the formation of a fused Ir nano-network on TiO₂ supports reported here. This method makes it simple to scale up the Ir NN@TiO₂ generated to more than 5 g each batch (Fig. 1c).

As shown in the transmission electron microscopy (TEM) image (Fig. 1d) and N₂ adsorption–desorption isotherms (Fig. S5, ESI[†]), Ir NN@TiO₂ is composed of spatially interconnected nanoparticles with a particle size of *ca.* 1.2 nm, and has a large BET surface area of 43 m² g⁻¹. The high-resolution TEM result confirms that the Ir nanoparticles as building blocks are connected *via* grain boundaries (GBs) to form a fused Ir nano-network on TiO₂ supports (Fig. 1e). The interplanar spacings of Ir NN@TiO₂, which are *ca.* 0.22 nm and 0.19 nm, are attributed to the (111) and (200) crystallographic planes of face-centered-cubic (fcc) phase Ir. Element distribution analysis shows that Ir is highly dispersed on TiO₂ (Fig. S6, ESI[†]). The Ir loadings of both Ir NN@TiO₂ and Ir NP@TiO₂ are around 30 wt%, which are checked by the inductively coupled plasma atomic emission spectroscopy (ICP-OES). The Ir NN@TiO₂ presents a high electrical conductivity with over 0.2 S cm⁻¹ (Fig. 1f), which is 5 orders of magnitude higher compared with Ir NP@TiO₂. The result indicates that the fused Ir nano-network on TiO₂ supports largely enhance the electrical conductivity of the catalysts.

The powder X-ray diffraction (XRD) patterns of Ir NN@TiO₂ and Ir NP@TiO₂ are shown in Fig. S7 (ESI[†]). Both Ir NN@TiO₂ and Ir NP@TiO₂ samples show the diffraction peaks of the TiO₂ support, and the broadened diffraction peaks of Ir at 40–45°, implying the very small size of Ir on TiO₂. We further measure Ti L-edge X-ray absorption near-edge structure (XANES) spectra of Ir NN@TiO₂, Ir NP@TiO₂ and TiO₂ (Fig. 2a). Both these spectra feature L₂ and L₃ doublets, which arise from the electron excitation in Ti, specifically from Ti 2p_{1/2} and Ti 2p_{3/2} to unoccupied 3d orbitals, respectively. The L₂ and L₃ edges are

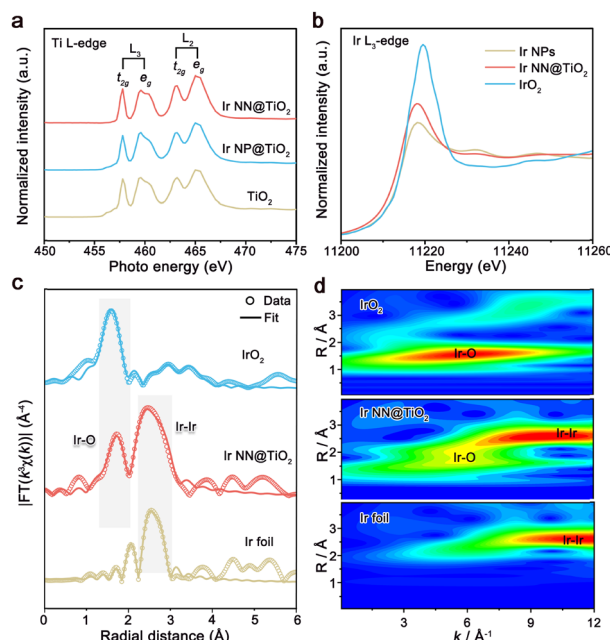


Fig. 2 (a) Ti L_{2,3}-edge XANES spectra for Ir NN@TiO₂, Ir NP@TiO₂ and TiO₂. (b) The Ir L₃-edge XANES and (c) EXAFS spectra for Ir NN@TiO₂, IrO₂ and Ir foil. (d) Wavelet transform-EXAFS Ir L₃-edge spectra for Ir NN@TiO₂, IrO₂ and Ir foil.

further divided into e_g and t_{2g} peaks as a result of crystal field splitting in an octahedral symmetry.¹⁴ The relative intensity and peak position of Ir NN@TiO₂ and Ir NP@TiO₂ in the L₂ and L₃ band are almost the same as those of TiO₂. These results indicate that the TiO₂ supports for Ir NN@TiO₂ and Ir NP@TiO₂ exhibit no essential differences, and the much higher electrical conductivity of Ir NN@TiO₂ is originated from the fused Ir nano-network.

The electronic structure and local coordination environment of the Ir were investigated by X-ray absorption spectroscopy. The maximum of the absorption peak of Ir NN@TiO₂ is shifted to a higher energy value compared to metallic Ir from the Ir L₃-edge XANES spectra (Fig. 2b), indicating the formation of iridium oxide layer on the Ir NN@TiO₂ surface. In the Fourier transforms of the extended X-ray absorption fine structure (EXAFS) at the Ir L₃-edge (Fig. 2c and Table S1, ESI[†]), there are two prominent peaks for Ir NN@TiO₂, which correspond to the Ir–Ir bond and the Ir–O bond. The wavelet transform analysis (Fig. 2d) also exhibits the atomic distances for both Ir–Ir and Ir–O. In addition, the surface oxidation of Ir for Ir NN@TiO₂ is further supported by X-ray photoelectron spectroscopy (XPS, Fig. S8 in ESI[†]), which shows a mixed oxidation state of Ir⁰ and Ir⁴⁺ for Ir NN@TiO₂.

The electrocatalytic activity of Ir NN@TiO₂ for the OER was then assessed with a standard three-electrode cell in acidic solution (0.1 M HClO₄, see Experimental section in ESI[†]). For comparison, the same test conditions were used to evaluate the electrocatalytic activities of Ir NP@TiO₂ and unsupported Ir NPs (see Experimental section in ESI[†] for synthetic details). The polarization curves of the Ir NN@TiO₂, Ir NP@TiO₂ and Ir NPs are shown in Fig. 3a. The Ir NN@TiO₂ requires a lower overpotential (285 mV) than Ir NP@TiO₂ (297 mV) and Ir NPs



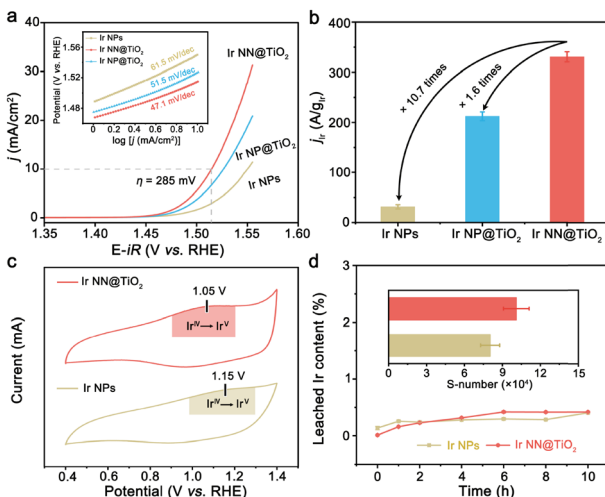


Fig. 3 (a) Electrochemical polarization curves for the OER in 0.1 M HClO_4 solution. The inset shows the Tafel plots for the OER over Ir NN@TiO₂, Ir NP@TiO₂ and Ir NPs. (b) Comparison of the Ir mass activity of Ir NN@TiO₂, Ir NP@TiO₂ and Ir NPs at 1.55 V vs. RHE. (c) CV curves obtained with Ir NN@TiO₂ and Ir NPs between 0.4 and 1.4 V vs. RHE. (d) The amounts (wt%) of leached Ir from Ir NN@TiO₂ and Ir NPs during the OER at 1.53 V vs. RHE. The inset shows S number of two catalysts after 10 h of electrocatalysis.

(321 mV) in order to reach a 10 mA cm^{-2} current density. Hence, Ir NN@TiO₂ is a better electrocatalyst than Ir NP@TiO₂ and Ir NPs for the OER. The better activity of Ir NP@TiO₂ is consistent with its smaller Tafel slope (Fig. 3a, inset). The former gives a lower value of 47.1 mV dec^{-1} than those measured by Ir NP@TiO₂ (51.5 mV dec^{-1}) and Ir NPs (61.5 mV dec^{-1}). At 1.55 V *versus* reversible hydrogen electrode (RHE), Ir NN@TiO₂ presents an Ir mass activity of $331 \text{ A g}_{\text{Ir}}^{-1}$ (Fig. 3b), which is about 1.6 and 10.7 times more than that of the Ir NP@TiO₂ ($212 \text{ A g}_{\text{Ir}}^{-1}$) and Ir NPs ($31 \text{ A g}_{\text{Ir}}^{-1}$).

To further compare the specific activities of Ir NN@TiO₂ and Ir NPs, the electrochemical surface areas (ECSAs), which are calculated from the electrochemical double-layer capacitance value,¹⁵ were used to normalize the measured currents (Fig. S9 in ESI[†]). The specific activity (j_{ECSA}) of Ir NN@TiO₂ is approximately 8.9 times higher than that of Ir NPs at 1.55 V, suggesting the higher intrinsic activity of Ir NN@TiO₂. We investigate cyclic voltammetry (CV) curves of Ir NN@TiO₂ and Ir NPs in a potential range from 0.4 to 1.4 V *vs.* RHE, prior to OER potential (Fig. 3c). The redox peak between 1.1 V and 1.2 V *vs.* RHE is identified to the $\text{Ir}^{IV}/\text{Ir}^V$ redox peaks.¹⁶ Compared with Ir NPs, the $\text{Ir}^{IV}/\text{Ir}^V$ redox peak of Ir NN@TiO₂ shifts to a lower potential, allowing Ir NN@TiO₂ to catalyze the OER more efficiently. The low redox peak potential and high intrinsic activity of Ir NN@TiO₂ can be attributed to the high coverage of surface hydroxyl groups, as supported by Fourier transform infrared spectroscopy (Fig. S10, ESI[†]). Ir NN@TiO₂ demonstrates remarkable stability at a 10 mA cm^{-2} current density, maintaining catalytic performance for over 200 h without significant fluctuation (Fig. S11, ESI[†]). Ir NN@TiO₂ delivers nearly 100% faradaic efficiency (Fig. S12, ESI[†]), indicating that the current measured is exclusively used for the OER.

To study structural stability, ICP-OES experiments were performed to monitor the quantity of Ir ion dissolution in the electrolyte during the OER. The amount of dissolved Ir ions for Ir NN@TiO₂ is close to that for Ir NPs during 10 h electrocatalysis for the OER (Fig. 3d). Subsequently, we calculate the stability number to study structural stability,¹⁶ which represents the number of O_2 molecules generated per iridium atom dissolution (Fig. 3d, inset). The Ir NN@TiO₂ presents a higher S-number (1.0×10^5) than the Ir NPs (8.8×10^4). Moreover, there is negligible Ti leaching (0.03 wt%) from Ir NN@TiO₂ during the OER. We further characterized Ir NN@TiO₂ after the OER. The SEM and TEM images show that Ir NN@TiO₂ retains the original morphology after the OER (Fig. S13, ESI[†]). We compare the L_3 -edge EXAFS spectra (Fig. S14, ESI[†]) and XRD patterns (Fig. S15, ESI[†]) for Ir NN@TiO₂ before and after the OER. There is an obvious electrochemical oxidation of Ir during the acidic OER.

We used an Ir NN@TiO₂ catalyst as the anode catalyst, 40% Pt/C as the cathode catalyst, and Nafion 115 membrane as the PEM (thickness = 125 μm) to assemble a single cell PEMWE with a 5 cm^2 working area (Fig. 4a). The CCM is prepared by an ultrasonic spraying method. ICP-OES indicates that the Ir and Pt loadings are regulated to $0.30 \text{ mg}_{\text{Ir}} \text{ cm}^{-2}$ and $0.44 \text{ mg}_{\text{Pt}} \text{ cm}^{-2}$. According to the SEM image of CCM, both Ir NN@TiO₂ and Pt/C on the PEM surface generate evenly distributed agglomerates with a thickness of around 2 μm for the anode and 10 μm for the cathode catalyst layers (Fig. S16, ESI[†]). For comparison, the PEMWEs using Ir NP@TiO₂ and Ir NP anodes are assembled under the same conditions.

As shown in Fig. 4b, the polarization curve of PEMWE using Ir NN@TiO₂ delivers 2.9 and 3.6 A cm^{-2} current densities at cell voltages of 1.9 and 2.0 V at 80 °C. The performance is significantly superior to those PEMWEs using the Ir NP@TiO₂ anode (2.3 A cm^{-2} @ 1.9 V) and Ir NPs anode (1.8 A cm^{-2} @ 1.9 V). Notably, the Ir NN@TiO₂-based cell's performance surpasses the majority of previously reported PEMWEs that use efficient Ir-based anode electrocatalysts (Fig. 4c and Table S2, ESI[†]), including supported catalysts (*e.g.*, Ir@WO_x, IrO₂@TaB₂ and IrO₂@TiN_{1+x}) and solid solution catalysts (*e.g.*, Ta_{0.1}Tm_{0.1}Ir_{0.8}O₂, W_{0.7}Ir_{0.3}O_y and Ir_{0.7}Ru_{0.3}O₂).^{17–22}

To explore the reasons behind the excellent performance of the Ir NN@TiO₂-based cell, we examine the contributions of three main causes of total voltage losses in a PEMWE: ohmic overvoltage, transport overvoltage, and kinetic overvoltage (Fig. S17–S19, ESI[†]).²³ For comparison, we also calculate the voltage loss components for cells based on Ir NP@TiO₂ and Ir NPs (Fig. S20, ESI[†]). As shown in Fig. 4d, the kinetic overvoltage for the Ir NN@TiO₂-based cell is lower than that of Ir NP-based cells, attributed to the higher activity of the Ir NN@TiO₂ catalyst. The ohmic overvoltage of the Ir NN@TiO₂-based cell is significantly reduced compared to the Ir NP@TiO₂-based cell, thanks to its superior electrical conductivity. In addition, the transport overpotential of the Ir NN@TiO₂ anode cell is much smaller than that of the Ir NP anode cell, indicating favorable transport of O_2 and water within the CCM. Taken together, these results highlight that both the optimal reaction kinetics, high

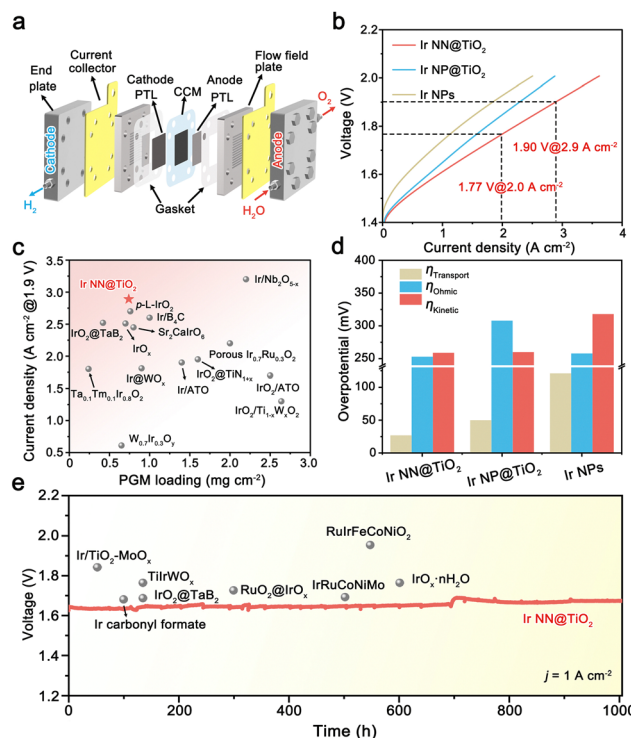


Fig. 4 (a) Schematic diagram of PEMWE. (b) Polarization curves of PEMWE using Ir NN@TiO₂, Ir NP@TiO₂ and Ir NPs anodes. (c) Comparison of the performance of PEMWEs using different Ir-based catalysts. (d) The comparison of ohmic, transport, and kinetic losses for PEMWEs using Ir NN@TiO₂, Ir NP@TiO₂ and Ir NPs anodes. (e) Chronopotentiometry curve of PEMWE using the NN@TiO₂ anode at 1 A cm⁻² current density.

electrical conductivity and efficient mass transport are essential for achieving high-performance PEMWE for Ir NN@TiO₂.

The stability of CCM is a crucial factor for the practical use of PEMWE. To assess the long-term catalytic stability, we conducted a chronopotentiometry measurement for the Ir NN@TiO₂-based cell at a steady 1 A cm⁻² current density (Fig. 4e). The electrocatalytic durability of PEMWEs using recently developed Ir-based anode catalysts is generally under 500 h (Table S3, ESI[†]). By comparison, the Ir NN@TiO₂-based cell exhibits nearly unchanged electrocatalytic performance over 1000 hours, with an average degradation rate of 30.8 μ V h⁻¹, indicating its remarkable catalytic stability.

In conclusion, Ir NN@TiO₂ possesses not only high intrinsic activity and high structural stability for the acidic OER but also high electrical conductivity. The PEMWE using the Ir NN@TiO₂ anode delivers 2.9 A cm⁻² current density at a cell voltage of 1.9 V with a low Ir content of 0.3 mg_{Ir} cm⁻², while giving excellent activity retention at 1 A cm⁻² for over 1000 hours. This performance represents one of the highest levels reported for PEMWEs.

This work was supported by the State Grid Headquarter Science and Technology project (5419-202158490A-0-5-ZN).

Data availability

The data supporting this article have been included as part of the ESI.[†]

Conflicts of interest

There are no conflicts to declare.

Notes and references

- 1 M. Chatenet, B. G. Pollet, D. R. Dekel, F. Dionigi, J. Deseure, P. Millet, R. D. Braatz, M. Z. Bazant, M. Eikerling, I. Staffell, P. Balcombe, Y. Shao-Horn and H. Schäfer, *Chem. Soc. Rev.*, 2022, **51**, 4583–4762.
- 2 Y. Wang, Y. Pang, H. Xu, A. Martinez and K. S. Chen, *Energy Environ. Sci.*, 2022, **15**, 2288–2328.
- 3 Q. Wu, Y. Wang, K. Zhang, Z. Xie, K. Sun, W. An, X. Liang and X. Zou, *Mater. Chem. Front.*, 2023, **7**, 1025–1045.
- 4 Q. Liu, K. Liu, J. Huang, C. Hui, X. Li and L. Feng, *Dalton Trans.*, 2024, **53**, 3959–3969.
- 5 R.-T. Liu, Z.-L. Xu, F.-M. Li, F.-Y. Chen, J.-Y. Yu, Y. Yan, Y. Chen and B. Y. Xia, *Chem. Soc. Rev.*, 2023, **52**, 5652–5683.
- 6 K. Zhang, X. Liang, L. Wang, K. Sun, Y. Wang, Z. Xie, Q. Wu, X. Bai, M. S. Hamdy, H. Chen and X. Zou, *Nano Res. Energy*, 2022, **1**, 9120032.
- 7 R. J. Ouimet, J. R. Glenn, D. De Porcellinis, A. R. Motz, M. Carmo and K. E. Ayers, *ACS Catal.*, 2022, **12**, 6159–6171.
- 8 Z. Shi, J. Li, J. Jiang, Y. Wang, X. Wang, Y. Li, L. Yang, Y. Chu, J. Bai, J. Yang, J. Ni, Y. Wang, L. Zhang, Z. Jiang, C. Liu, J. Ge and W. Xing, *Angew. Chem., Int. Ed.*, 2022, **61**, e202212341.
- 9 H. Yu, Y. Ji, C. Li, W. Zhu, Y. Wang, Z. Hu, J. Zhou, C.-W. Pao, W.-H. Huang, Y. Li, X. Huang and Q. Shao, *J. Am. Chem. Soc.*, 2024, **146**, 20251–20262.
- 10 Y. N. Regmi, E. Tzanetopoulos, G. Zeng, X. Peng, D. I. Kushner, T. A. Kistler, L. A. King and N. Danilovic, *ACS Catal.*, 2020, **10**, 13125–13135.
- 11 J. Islam, S.-K. Kim, P. T. Thien, M.-J. Kim, H.-S. Cho, W.-C. Cho, C.-H. Kim, C. Lee and J. H. Lee, *J. Power Sources*, 2021, **512**, 230506.
- 12 C. Baik, J. Cho, J. I. Cha, Y. Cho, S. S. Jang and C. Pak, *J. Power Sources*, 2023, **575**, 233174.
- 13 H. W. Park, B. G. Seo, J. W. Shim, N. Il Kim, Y. S. Choi and J. H. Shim, *Appl. Catal. B*, 2023, **337**, 122956.
- 14 L. Pan, M. Ai, C. Huang, L. Yin, X. Liu, R. Zhang, S. Wang, Z. Jiang, X. Zhang, J.-J. Zou and W. Mi, *Nat. Commun.*, 2020, **11**, 418.
- 15 S. Trasatti and O. A. Petrii, *Pure Appl. Chem.*, 1991, **63**, 711–734.
- 16 S. Geiger, O. Kasian, M. Ledendecker, E. Pizzutilo, A. M. Mingers, W. T. Fu, O. Diaz-Morales, Z. Li, T. Oellers, L. Fruchter, A. Ludwig, K. J. J. Mayrhofer, M. T. M. Koper and S. Cherevko, *Nat. Catal.*, 2018, **1**, 508–515.
- 17 M. Faustini, M. Giraud, D. Jones, J. Rozière, M. Dupont, T. R. Porter, S. Nowak, M. Bahri, O. Ersen, C. Sanchez, C. Boissière, C. Tard and J. Peron, *Adv. Energy Mater.*, 2019, **9**, 1802136.
- 18 S. Hao, H. Sheng, M. Liu, J. Huang, G. Zheng, F. Zhang, X. Liu, Z. Su, J. Hu, Y. Qian, L. Zhou, Y. He, B. Song, L. Lei, X. Zhang and S. Jin, *Nat. Nanotechnol.*, 2021, **16**, 1371–1377.
- 19 G. Jiang, H. Yu, Y. Li, D. Yao, J. Chi, S. Sun and Z. Shao, *ACS Appl. Mater. Interfaces*, 2021, **13**, 15073–15082.
- 20 S. Wang, H. Lv, S. Bi, T. Li, Y. Sun, W. Ji, C. Feng and C. Zhang, *Mater. Chem. Front.*, 2021, **5**, 8047–8055.
- 21 Y. Wang, M. Zhang, Z. Kang, L. Shi, Y. Shen, B. Tian, Y. Zou, H. Chen and X. Zou, *Nat. Commun.*, 2023, **14**, 5119.
- 22 T. Yan, S. Chen, W. Sun, Y. Liu, L. Pan, C. Shi, X. Zhang, Z.-F. Huang and J.-J. Zou, *ACS Appl. Mater. Interfaces*, 2023, **15**, 6912–6922.
- 23 Z. Kang, M. Wang, Y. Yang, H. Wang, Y. Liu, J. Mo, J. Li, P. Deng, C. Jia and X. Tian, *Int. J. Hydrogen Energy*, 2022, **47**, 5807–5816.

